115-145 GHz STABLE DEPLETION LAYER SECOND-HARMONIC TRANSFERRED ELECTRON OSCILLATORS

M.F. Zybura, S.H. Jones, J.E. Carlstrom†, and J.D. Crowley‡
Applied Electrophysics Laboratories
Department of Electrical Engineering
University of Virginia
Charlottesville, VA 22903-2442
†Department of Astrophysics
California Institute of Technology
Pasadena, CA 91125
‡Litton Solid State
Santa Clara, CA 95054-3095

Abstract

The aim of this paper is to demonstrate and clarify the superior performance of Transferred Electron Devices utilizing current limiting contacts. These devices operate in a novel Stable Depletion Layer mode characterized by an oscillating stable depletion layer rather than an unstable propagating accumulation layer or dipole. A small-signal model is offered to explain the stable small-signal resistance of the device over a broad frequency range. Large-signal analysis is completed using a hydrodynamic device simulator employing the temperature-dependent drift/diffusion equation and Poisson's equation combined with a novel harmonic-balance circuit analysis technique. Analysis of the electric fields, electron concentration, and device temperature is included for steady-state large-signal operation. Embedding impedances are extracted for a broadband cavity using the High Frequency Structure Simulator from Hewlett Packard. Comparisons are made with experimental data for a Stable Depletion Layer oscillator in the above mentioned broadband continuously tunable cavity with excellent correlation, demonstrating at least 30 mW from 115-145 GHz. High reliability operation and as much as 60 mW of output power at 140 GHz is achievable.

1 Introduction

Presently, the state-of-the-art performance in Transferred Electron Devices (TEDs) is dominated by current limiting devices demonstrating 60 mW at 140 GHz [1]. In comparison to typical TEDs, current limiting TEDs offer increased output power, reliability, and improved frequency stability with temperature variation. The salient feature of these devices is a current limiting contact applied directly to the active layer of the device. The resulting shallow barrier contacting interface establishes a depletion layer at the cathode in the active region; the magnitude of this depletion layer governs the operating mode of the device. As a result of the cathode depletion, these devices operate in a novel Stable Depletion Layer (SDL) mode characterized by an oscillating stable depletion layer rather than an unstable propagating accumulation layer or dipole. This phenomena was first described by Kroemer [2], but its application to high performance oscillators was not fully recognized at that time. Essentially, the SDL mode is a stable negative resistance mode which is rich in both fundamental and second-harmonic frequency components. Since the output power is no longer limited by the formation of large charge instabilities, a higher frequency of operation is possible. Current limiting TEDs also exhibit much lower operating current densities, temperatures, and thus higher reliability performance.

2 Small-Signal Analysis

The approximate behavior of current limiting TEDs can be obtained through a small-signal analysis [2] of the commercially available Litton Solid State second-harmonic InP TED of reference [1]. The device structure consists of a current limiting contact applied to a 1.8 μm InP active region uniformly doped at $1x10^{16}$ cm^{-3}, followed by an n$^+$ anode region. Typical d.c. bias points range from -10 V$\leq V_{d.c.} \leq$-7 V. Each physical quantity characterizing the semiconductor is written as a sum of a time-independent term and a small oscillating term:

$$E = E_o + E_1 e^{i\omega t},$$

$$n = n_o + n_1 e^{i\omega t},$$

$$v = v_o + v_1 e^{\imath\omega t}, \tag{1}$$

where E, n, v, and ω, are the electric field, the electron concentration, the electron velocity, and the angular frequency, respectively. If higher order terms are neglected, the continuity equation for the oscillating part of the total current can be written as

$$\begin{aligned} J_1 &= q(n_1 v_o + n_o v_1) + \imath\omega\epsilon E_1 \\ &= \epsilon v_o \frac{\partial E_1}{\partial x} + (\sigma + \imath\omega\epsilon) E_1 = constant, \end{aligned} \tag{2}$$

where σ is the small-signal differential conductivity, ϵ is the dielectric permittivity, and Poisson's equation is used to generate the first term to the right of the equality. The oscillating current density at the cathode, $x = 0$, is given by

$$J_1(0) = [\sigma(0) + \imath\omega\epsilon] E_1(0), \tag{3}$$

and the cathode small-signal differential conductivity, $\sigma(0)$, is approximated as

$$\begin{aligned} \sigma(0) &= \frac{\partial J_c(0)}{\partial E_1} \\ &\simeq \frac{\partial}{\partial E_1} q\mu E n(0) [exp(\frac{qV}{kT}) - 1] \\ &\simeq -q\mu n(0), \end{aligned} \tag{4}$$

for transport across shallow metal-semiconductor barriers ($<$ 300 meV) [3]. The exponential term in equation (4) has been neglected since the diode is strongly reverse biased under normal operating conditions. In this equation, μ, k, and T are the electron mobility, Boltzmann's constant, and the lattice temperature, respectively. The electron concentration at the cathode, $n(0)$, is given by

$$n(0) = N_c exp(-\frac{q\phi_b}{kT}), \tag{5}$$

where N_c is the effective density of states in the conduction band, and ϕ_b is the barrier height. To complete the analysis, several approximations are needed. An average carrier velocity, $\overline{v}$, is defined as $\overline{v} = (v_{peak} + v_{sat})/2$. This average velocity is employed since the applied d.c. bias results in an electric field profile which is approximately equal to that of the peak field at the anode and substantially greater

than the peak field at the cathode. The small-signal differential conductivity, σ, of (2) is assigned an average value

$$\overline{\sigma} = q\overline{n_o}\overline{\frac{dv}{dE}} \tag{6}$$

where

$$\overline{n_o} = \frac{n(0)}{2}(1 + \frac{v_{sat}}{v_{peak}}), \tag{7}$$

and $\overline{dv/dE}$ is approximated as the value midway between the peak and saturation velocities. The solution of (2) subject to the boundary condition (4) is

$$E_1(x) = \frac{J_1}{\overline{\sigma} + \imath\omega\epsilon}[1 - \frac{\sigma(0) - \overline{\sigma}}{\sigma(0) + \imath\omega\epsilon}e^{\imath\Gamma x}], \tag{8}$$

where

$$\Gamma = -\frac{\overline{\sigma} + \imath\omega\epsilon}{\epsilon\overline{v}}. \tag{9}$$

The impedance then is found to be

$$\begin{aligned} Z &= \frac{1}{J_1}\int_0^l E_1 dx \\ &= \frac{l}{\overline{\sigma} + \imath\omega\epsilon}[1 - \frac{\sigma(0) - \overline{\sigma}}{\sigma(0) + \imath\omega\epsilon}\frac{e^{\Gamma l} - 1}{\Gamma l}](\Omega - cm^2). \end{aligned} \tag{10}$$

There are two distinct contributions to Z, a uniform field contribution, and a space-charge wave contribution proportional to $\sigma(0) - \overline{\sigma}$. The small-signal resistance and reactance for the InP TED of reference [1] are shown in Figures 1 and 2, respectively, for several cathode barrier heights.

As illustrated in Figure 1, both the magnitude and region of negative resistance is greatly dependent on the cathode barrier, ϕ_b. With a cathode barrier of 110 meV, there exists a large region of negative resistance from 25 to 85 GHz to support fundamental oscillations. As the cathode barrier is increased such regions quickly are damped to near zero resistance over the frequency range of interest. The small-signal reactance is primarily capacitive with a slight oscillatory behavior. As the cathode barrier height is increased, the magnitude of the reactance is skewed to a lower frequency with smaller oscillations at the higher frequencies. Although not shown, changing the active region length provides further control over the region and magnitude of negative resistance. For example, a 1.5μm active region results in a

negative resistance domain ($\leq -1\Omega$) from 25-100 GHz, while a 1.9μm active region yields negative resistance from 21-75 GHz. While approximations to the average velocity and conductivity here are quite crude, similar trends are predicted by the large-signal simulator, described below, under small-signal a.c. drive.

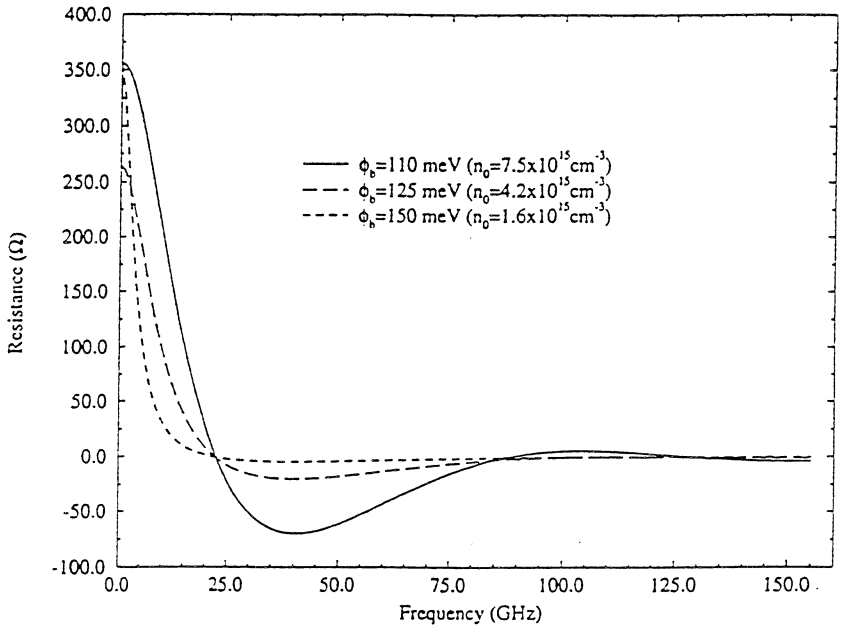

Figure.1: Small-signal resistance versus frequency for the Litton second-harmonic InP TED.

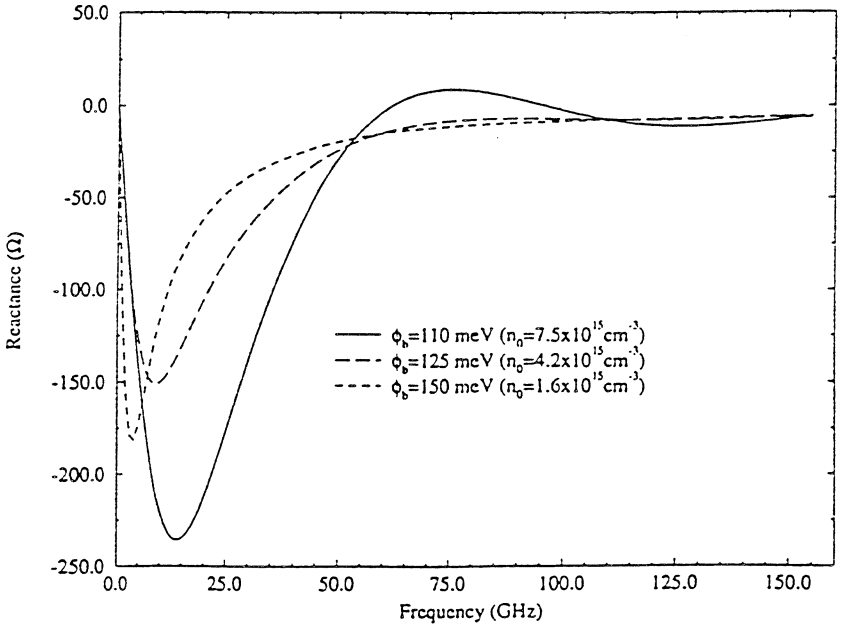

Figure 2: Small-signal reactance versus frequency for the Litton second-harmonic InP TED.

3 Combined Drift and Diffusion/Harmonic-Balance Large-Signal Simulation

A dynamic understanding of current limiting contact TEDs can be obtained through combined Drift and Diffusion/Harmonic-Balance (DDHB) simulations of the Litton InP second-harmonic TED mounted in a broadband cavity (H63) similar to that of reference [4]. The embedding impedances of the circuit have been extracted using the High Frequency Structure Simulator (HFSS) [5], and comparisons with experimental results have been made. The DDHB analysis used here employs an efficient fixed-point iteration method [6] derived from the multiple-reflection technique [7], facilitating the use of a hydrodynamic device simulator using the temperature-dependent drift/diffusion equation and Poisson's equation [8]. The drift and diffusion equation utilizes both field- (0.1-100 kV/cm) and temperature- (300-500 K) dependent mobility and diffusivity extracted from Monte Carlo simulations, and is coupled to a thermal analysis that includes all regions of the packaged device [9]. Complex frequency-dependent parasitic impedances, external to the active region of the device and similar to those of [10], are included in the analysis as additional contributions to the linear device embedding circuit. The Dirichlet boundary condition for electron concentration at the cathode, $n(0)$, is adjusted according to the current limiting contact barrier height for the SDL TEDs (see equation 5).

Figure 3 shows the current and voltage waveforms for the second-harmonic InP TED at 140 GHz in the H63 cavity where $\phi_b \approx 110$ meV, $n(0) \approx 7x10^{15}\text{cm}^{-3}$. Since the fundamental oscillation (70 GHz) is cutoff and terminated in an essentially reactive load, the fundamental voltage is large, and the corresponding fundamental output power is near zero. At 140 GHz second-harmonic operation, the magnitude of the fundamental voltage is 8.8 V, and the fundamental embedding impedance is $Z_1^{ckt} = 0.1 + \imath 12.3\Omega$. The second-harmonic embedding impedance, extracted from HFSS simulations at 140 GHz for the optimal backshort positions, is $Z_2^{ckt} = 12.0 + \imath 3.8\Omega$. The third-harmonic embedding impedance remains fairly stable at $Z_3^{ckt} = 0.2 + \imath 59.9\Omega$ throughout the frequency range of interest. The optimal d.c. bias ($-10 \leq V_{d.c.} \leq -7$

V) is nearly twice that of a conventional Gunn diode of similar length, and the resultant d.c. current is more than three times smaller. Consequently, the SDL TED operating temperature over the active layer is nearly 100°C cooler than a companion (n^+nn^+) Gunn diode, leading to both better reliability and performance.

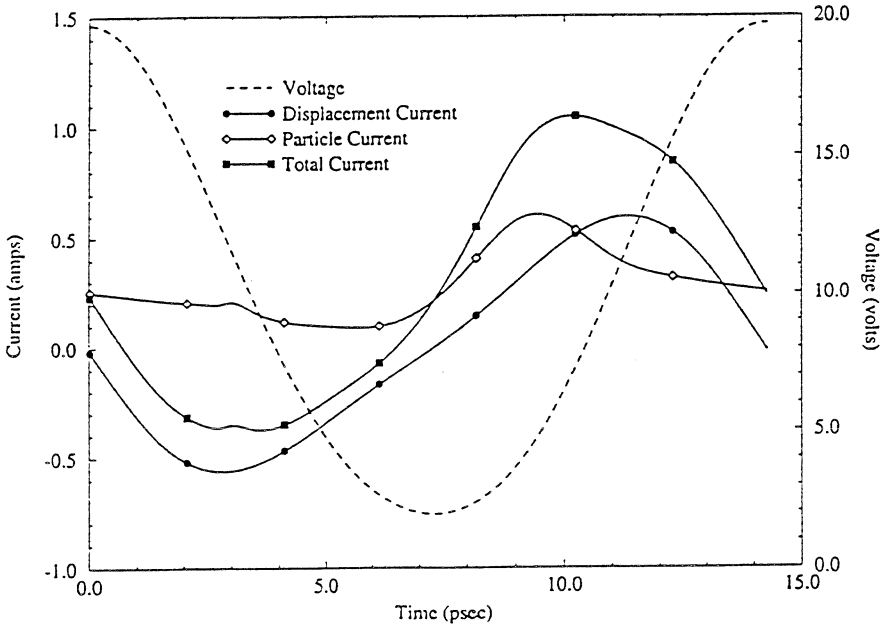

Figure 3: Current and voltage waveforms for the Litton second-harmonic InP SDL TED at 140 GHz. ($V_{d.c.} = -10V$, $Z_1^{ckt} = 0.17 + \imath 12.3\Omega$, $Z_2^{ckt} = 12.0 + \imath 3.8\Omega$)

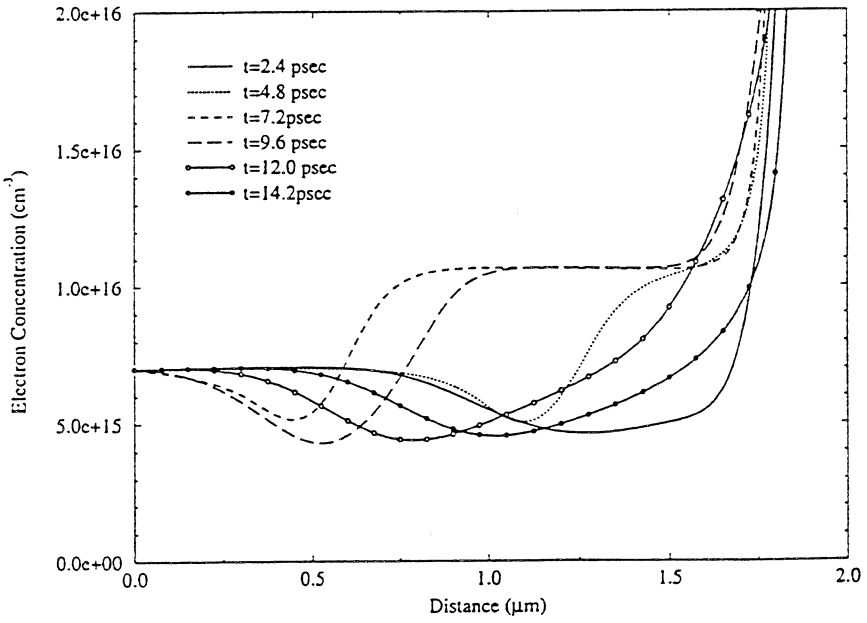

Figure 4: Electron concentration (positive electron charge) versus distance and time for the Litton second-harmonic InP SDL TED at 140 GHz. ($V_{d.c.} = -10V$, $Z_1^{ckt} = 0.17 + \imath 12.3\Omega$, $Z_2^{ckt} = 12.0 + \imath 3.8\Omega$)

Figures 4 and 5 show the corresponding electron concentration and electric field versus distance and time. The positive space charge associated with the partial electron depletion at the cathode leads to a decreasing electric field with increasing distance from the cathode and, thus, no possibility of accumulation layer formation. Like Gunn diodes, the method of power generation is a combined transferred electron and transit time effect. The power is generated by the transferred electron effect which serves to offset the current and voltage phase relation; the depletion layer transit time effect reduces the power dissipation by suppressing the particle current during the decreasing voltage cycle. As the applied voltage increases from its minimum, the particle current is quenched due to the transferred electron effect since, at this point, the entire electric field profile across the active region moves above the peak field ($E_{peak}^{InP} \approx 12$ kV/cm). This occurs approximately 9.5ps into an oscillation cycle and is shown in Figures 3 and 5. The reduction in particle current is further aided by the

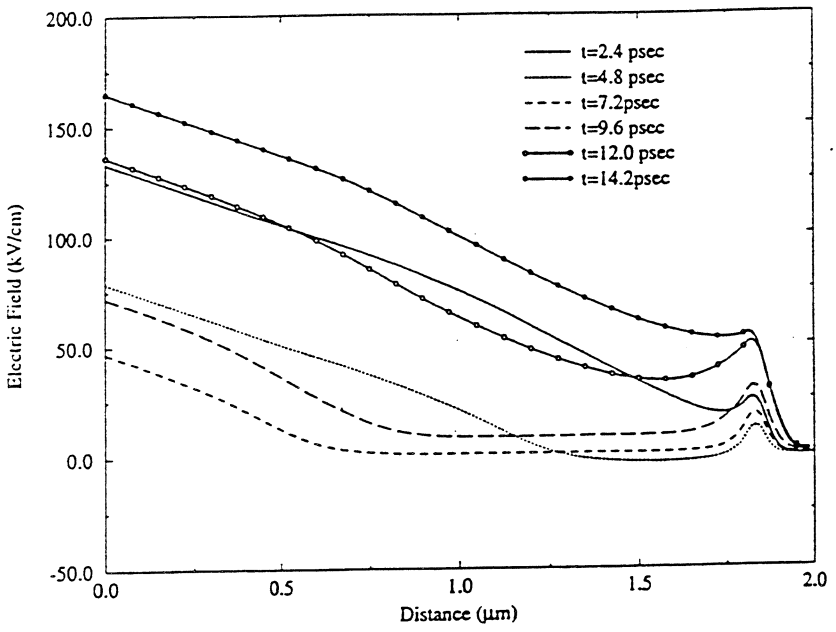

Figure 5: Electric field (positive electron charge) versus distance and time for the Litton second-harmonic InP SDL TED at 140 GHz. ($V_{d.c.} = -10V$, $Z_1^{ckt} = 0.17 + \imath 12.3\Omega$, $Z_2^{ckt} = 12.0 + \imath 3.8\Omega$)

onset of the partial depletion of the entire active region; this occurs at approximately 13ps into an oscillation cycle, and is maintained until midway between the peak and trough of the decreasing voltage waveform (3ps). As shown in Figure 4, a slight rise in particle current is seen at this point associated with the re-emergence of the depletion region from the anode. However, due to the large back diffusion of carriers from the anode, a minimal particle current is preserved. The resultant asymmetry in the current waveform provides excellent power generation at both the fundamental and second-harmonic.

Comparisons with experimental results have been made for the Litton second-harmonic InP SDL TED mounted in a broadband (115-145 GHz) cavity. More than 30 mW of CW output power can be obtained experimentally over the entire band. The cavity, shown in Figure 6, is similar to that of reference [4], with the diode embedded in a fundamental frequency resonator, and the second-harmonic power coupled out through half-height WR-8 waveguide having a cutoff frequency below the fundamental frequency (67.5-73.5 GHz). The fundamental resonator consists of a disk

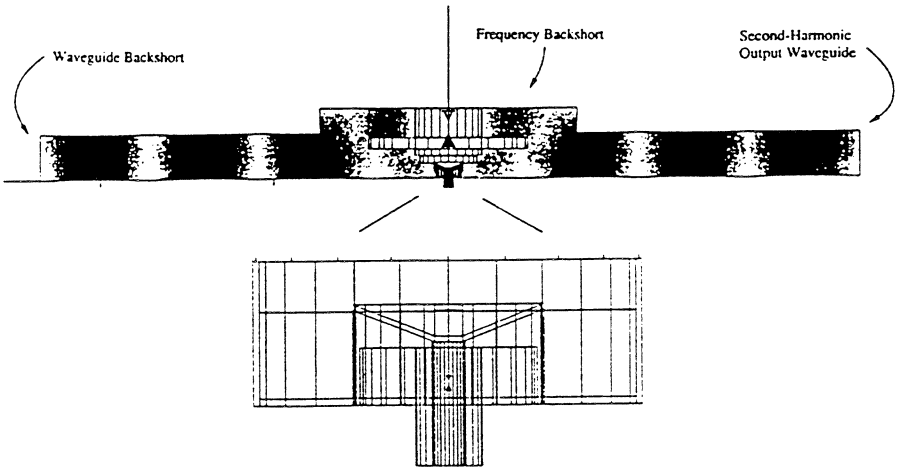

Figure 6: An HFSS schematic of the H63 115-145 GHz second-harmonic cavity and corresponding electric field profiles for 140 GHz operation. The package and coaxial probe are shown in the expanded region.

and post structure with a mechanically adjustable post length. An adjustable waveguide backshort is also provided to optimize the second-harmonic output power. Also shown in Figure 6 is a snapshot of the resultant electric field intensity at 140 GHz, and an expanded view of the diode package. For HFSS simulations, the cavity is characterized as a three port system in which both the second-harmonic output and backshort waveguides are modelled as matched loads. Excitations representing those generated by the diode occur through the third port via a coaxial line whose inner dimension is precisely that of the TED. Since the frequency backshort is adjacent to large evanescent fields, it is modelled physically by adjusting the height of the fundamental resonator according to experimental settings. The variable waveguide backshort is modelled through the use of the Microwave Design System (MDS) [11] using the simulated HFSS S-parameters. A variable length of matched transmission line, terminated in an electrical short, is added, and the input impedance at the diode port is extracted through standard transformation of the S-parameter matrix. Figure 7 shows the simulated 140 GHz second-harmonic embedding impedance ver-

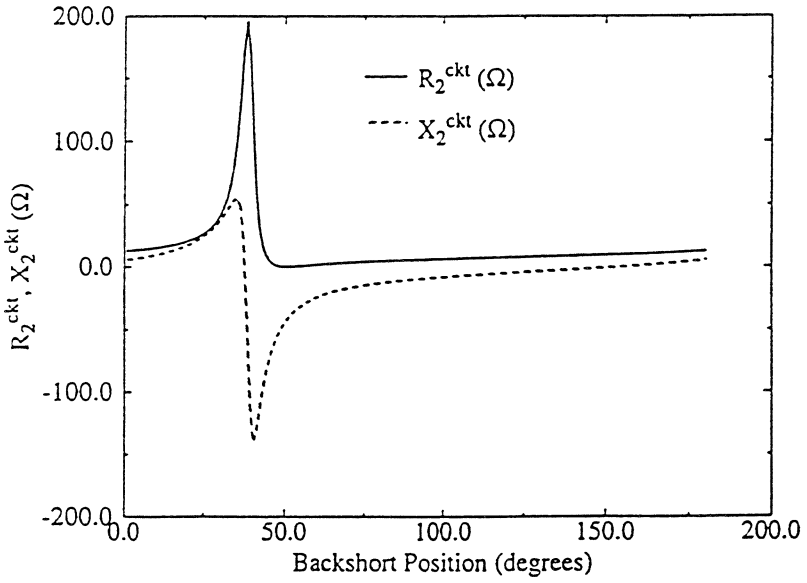

Figure 7: Simulated 140 GHz second-harmonic embedding impedances versus waveguide backshort position for the H63 broadband cavity.

sus waveguide backshort position for the H63 cavity. Besides a resonance at $\sim 40°$, the resistance, R_2^{ckt}, and reactance, X_2^{ckt}, remain quit low ($\leq 20\Omega$) throughout the tuning range. Both capacitive and inductive reactances can be presented to the diode at the second harmonic; substantially better performance is obtained with the latter. Combined drift and diffusion/harmonic balance simulations have been performed employing optimal backshort positions as derived from HFSS, and the results are shown in Table 1. It is important to note that this commercially available device outperforms conventional research oriented Gunn [12], IMPATT [13], and TUNNET [14] diodes even when presented with a wide range of second-harmonic embedding impedances associated with a broadband cavity. Experimentally, as much as 60 mW has been achieved at 140 GHz with optimal embedding impedances [1].

Frequency	125 GHz		130 GHz		140 GHz	
	Experiment	Simulation	Experiment	Simulation	Experiment	Simulation
$V_{d.c.}$ (V)	10	10	10	10	10	10
$I_{d.c.}$ (mA)	~ 220	279	~ 220	281	~ 220	278
$Z_1^{ckt}(\Omega)$	NA	$0.13 + \imath 13.9$	NA	$0.13 + \imath 13.1$	NA	$0.17 + \imath 12.3$
$Z_2^{ckt}(\Omega)$	NA	$4.1 + \imath 9.5$	NA	$10.9 + \imath 6.8$	NA	$12.0 + \imath 3.8$
Power (mW)	42	59	33	39	31	26

Table 1: 120-140 GHz second-harmonic InP SDL TED simulations versus experimental results from the H63 cavity ($Z_3^{ckt} = 0.2 + \imath 59.9\Omega$)

4 Conclusion

A novel Stable Depletion Layer TED operating mode representing state-of-the-art performance in low noise millimeter-wave power generation has been identified. In comparison to other solid-state millimeter-wave sources, SDL TEDs provide increased output power, reliability, and improved frequency stability with temperature variation. The small-signal negative resistance of SDL TEDs has been calculated, and large-signal simulations have provided a dynamic insight into the operation of this device. It has been shown that the SDL mode is a hybrid transferred electron/transit

time process. The phenomena and analysis reported here may also explain the behavior recently reported [15, 16] for low to high energy bandgap heterojunction cathode TEDs. Furthermore, simulations have been performed to show that significantly higher frequency (10 mW at 210 GHz) operation is possible since the output power is no longer limited by the formation of electron accumulation charge instabilities.

5 Acknowledgement

The authors would like to thank Dr. G. B. Tait of the United States Military Academy and Dr. D. Wilt of Nasa Lewis for stimulating discussions regarding TEOs and current limiting contacts. This work has been supported by NSF grant ECS-9202037.

References

[1] J. D. Crowley, C. Hang, R. E. Dalrymple, D. R. Tringali, F. B. Fank, L. Wandinger and H. B. Wallace, "140 GHz indium phosphide Gunn diode," *Electronics Lett.*, **30**, 6 (1994), pp. 499-500.

[2] H. Kroemer, "The Gunn Effect Under Imperfect Boundary Conditions," *IEEE Trans. Electron Devices*, vol. ED-15, No. 11, (1968), pp. 819-837.

[3] S. M. Sze, Physics of Semiconductor Devices. New York, NY: John Wiley & Sons, Inc. 1981.

[4] J. E. Carlstrom, R. L. Plambeck, and D. D. Thornton, "A Continuously Tunable 65-115-GHz Gunn Oscillator," *IEEE Trans. Microwave Theory Tech.*, vol. MTT-33, (1985) pp. 610-619.

[5] High Frequency Structure Simulator, Hewlett-Packard Co., Network Measurements Division, Santa Rosa, CA, 1992.

[6] G. B. Tait, "Efficient Solution Method for Unified Nonlinear Microwave Circuit and Numerical Solid-State Device Simulation," *IEEE Microwave and Guided Wave Let.*, Vol. 4, No. 12, (1994), pp. 420-422.

[7] P. H. Siegel, A. R. Kerr, and W. Hwang, "Topics in the Optimization of Millimeter-Wave Mixers," *NASA Tech. Paper*, No. 2287, March 1984.

[8] M. F. Zybura, S. H. Jones, G. B. Tait, and J. R. Jones, "100-300 GHz Gunn Oscillator Simulation Through Harmonic Balance Circuit Analysis Linked to a Hydrodynamic Device Simulator," *IEEE Microwave and Guided Wave Let.*, Vol. 4, No. 8, (1994), pp. 282-284.

[9] M. F. Zybura, S. H. Jones, G. B. Tait, and J. M. Duva, "Efficient Computer Aided design of GaAs and InP Millimeter Wave Transferred Electron Devices Including Detailed Thermal Analysis," *Solid-State Electronics*, Vol. 38, (1995), pp. 873-880.

[10] S. A. Maas Nonlinear Microwave Circuits: Artech House, Norwood, MA, 1988, Ch. 2, pp. 49-51.

[11] Microwave Design System, Hewlett-Packard Co., Network Measurements Division, Santa Rosa, CA, 1990.

[12] A. Rydberg, "A Contribution to the Design of Wideband Tunable Second Harmonic Mode Millimeter-Wave InP-TED Oscillators Above 110 GHz," *Intl. Journ. of Infrared and Millimeter Waves*, Vol. 11, No. 3, (1990), pp. 383-404.

[13] M. Tschernitz and J. Freyer, "Design and Realization of GaAs D-Band IMPATT Oscillators", *Proc.Fifth Intl. Symp. on Space THz Tech.*, Ann Arbor, Mi. May 10-12 (1994), pp. 611-621.

[14] H. Eisele and G. I. Haddad, "GaAs TUNNET Diodes on Diamond Heat Sinks for 100 GHz and Above," *IEEE Trans. Microwave Theory Tech.*, Vol. 43, No. 1, (1995), pp. 210-213.

[15] M. R. Friscourt, P. A. Rolland, and M. Pernisek, "Heterojunction Cathode Contact Transferred-Electron Oscillators," *IEEE Elec. Dev. Let.*, Vol. 6, No. 10, (1985), pp. 497-499.

[16] R. Kamoua, "Heterojunction Cathode Injectors for D-Band InP Gunn Devices," *Solid-State Electronics*, Vol. 38, No. 2, (1995), pp. 269-274.